Coherent Exciton Dynamics in Supramolecular Light-Harvesting Nanotubes Revealed by Ultrafast Quantum Process Tomography

Coherent exciton dynamics in supramolecular light-harvesting nanotubes revealed by ultrafast quantum process tomography

Joel Yuen-Zhou[1], Dylan H. Arias[1,2], Dorthe M. Eisele[1,2], Colby P. Steiner[1,2],
Jacob J. Krich[3], Moungi Bawendi[1,2], Keith A. Nelson[1,2] and Alán Aspuru-Guzik[1,4]
[1]*Center for Excitonics, Research Laboratory of Electronics,*
Massachusetts Institute of Technology, Cambridge, MA, USA,
[2]*Department of Chemistry, Massachusetts Institute of Technology, Cambridge, MA, USA,*
[3]*Department of Physics, University of Ottawa, Ottawa, ON, Canada, and*
[4]*Department of Chemistry and Chemical Biology, Harvard University, Cambridge, MA, USA.*

Abstract

Long-lived exciton coherences have been recently observed in photosynthetic complexes via ultrafast spectroscopy, opening exciting possibilities for the study and design of coherent exciton transport. Yet, ambiguity in the spectroscopic signals has led to arguments for interpreting them in terms of the exciton dynamics, demanding more stringent tests. We propose a novel strategy, Quantum Process Tomography (QPT) for ultrafast spectroscopy, to reconstruct the evolving quantum state of excitons in double-walled supramolecular light-harvesting nanotubes at room temperature. The protocol calls for eight transient grating experiments with varied pulse spectra. Our analysis reveals unidirectional energy transfer from the outer to the inner wall excitons, absence of nonsecular processes, and an unexpected coherence between those two states lasting about 150 femtoseconds, indicating weak electronic coupling between the walls. Our work constitutes the first experimental QPT in a "warm" and complex system, and provides an elegant scheme to maximize information from ultrafast spectroscopy experiments.

Recently, there has been great excitement about the detection of long-lived coherent dynamics in natural light-harvesting photosynthetic complexes via two-dimensional spectroscopy [1–3]. This long-lived coherence has generated interest and debate about its role in the efficient design of light-harvesting and exciton transport in biological and artificial settings [4–7]. These discussions have highlighted the importance of correctly interpreting the spectroscopic signals in terms of the microscopic dynamics in the material. The interplay between excitonic dynamics and vibrational dynamics can produce complex and potentially ambiguous spectroscopic signals, which can make extraction of information about exciton transport challenging [8–10]. Therefore, it is essential to develop methods to reliably extract the quantum dynamics of the interrogated material. In this article, we demonstrate the systematic characterization of the quantum dynamics of a condensed phase molecular system, namely, the excitons originating from the inner and outer walls of supramolecular light-harvesting nanotubes, via ultrafast Quantum Process Tomography (QPT) [11–13]. This manuscript is organized as follows: First, we briefly sketch the QPT formalism as a general method to maximize information from a quantum system interacting with its environment. Then, we describe the nanotubes and the optical setup, and explain how these two are ideally suited for the QPT protocol. Finally, we present the experimental data and its analysis, yielding a full characterization of the quantum dynamics of the excitonic system. To our knowledge, this article constitutes the first experimental realization of QPT on a molecular system in condensed phase, and provides general guidelines to adapt standard spectroscopic experiments to carry out QPT.

The time evolution of the excited state of an open quantum system (a system interacting with its environment, e.g., an electronic system interacting with an environment of vibrations) that is prepared by a pump pulse is, under general assumptions, given by [12–14],

$$\rho(T) = \chi(T)\rho(0), \tag{1}$$

where $\rho(T)$ is the density matrix of the system at time T after the pump pulse, and the *process matrix* $\chi(T)$ is a propagator that relates input and output states. By introducing a basis, Eq. (1) reads $\rho_{qp}(T) = \sum_{ij}\chi_{qpij}(T)\rho_{ij}(0)$, where $\chi_{qpij}(T)$ denotes a transition probability amplitude of ending in state $|q\rangle\langle p|$ at time T having started in state $|i\rangle\langle j|$. In other words, $\chi(T)$ characterizes the transfer processes amongst populations (diagonal elements of ρ) and coherences (off-diagonal elements of ρ). This phenomenology is familiar in nonlinear spectroscopy and can be discussed in terms of Double-Sided Feynman diagrams [15–17]. The process matrix $\chi(T)$ is a linear transformation of $\rho(0)$, which in turn yields the remarkable observation that, once $\chi(T)$ is given, the dynamics of the system are completely characterized; they are valid for arbitrary system initial states, including any interaction with the environment, whether characterized by Markovian or non-Markovian processes. The reconstruction of $\chi(T)$ is the central goal of QPT, an essential step in the verification of quantum technologies [18–26] and dynamical models. Determining $\chi(T)$ ensures that we have extracted the maximal amount of information possible about the excited state system dynamics. Previous theoretical work showed that selectively preparing and measuring a number of linearly independent initial states via laser excitation suffices to accomplish QPT [12, 13, 27, 28]. Hence, QPT can in principle be realized with the tools of ultrafast spectroscopy by collecting sufficient number of signals with varying frequency, polarization, and time delays. This work represents the first realization of QPT in a "warm" and complex system.

Results

We study the exciton states of light-harvesting nanotubes (Fig. 1a and SI Sec. 1) that self-assemble in a water/methanol solution from the amphiphilic cyanine dye monomer 3,3'-bis(2-sulfopropyl)-5,5',6,6'-tetrachloro-1,1'-dioctylbenzimidacarbocyanine [29] (abbreviated as C8S3) at room temperature (298 K). The nanotubes are about 10 nm in diameter, several micrometers long, and have a remarkably uniform supramolecular structure [30]: they are composed of two concentric cylinders—an inner wall cylinder and an outer wall cylinder—separated by about 4 nm [31, 32].

Upon self-assembly, the broad absorption band of the monomer (Fig. 1b) undergoes a large redshift of ~2,500 cm^{-1} reflecting the strong coupling of the molecular transition dipole moments forming delocalized excitonic eigenstates [33]. In addition, a complex pattern of absorption bands occurs, caused by the nanotube's complex cylindrical geometry [34, 35]. Bands (1) at $\sim 16600\,\mathrm{cm}^{-1}$ and (2) at $\sim 17100\,\mathrm{cm}^{-1}$ are polarized primarily parallel to the cylindrical axis and correspond to transitions which couple the Ground State Manifold (GSM, $|g\rangle$, state with no excitations) and the Single Exciton Manifold (SEM), composed of $|I\rangle$ and $|O\rangle$, that is, states that concentrate exciton amplitude mostly on the inner wall and the outer wall cylinders, respectively [36]. These transitions occur at $\omega_{Ig} \sim 16600\ \mathrm{cm}^{-1}$ and $\omega_{Og} \sim 17100\ \mathrm{cm}^{-1}$ ($\omega_{ij} = \omega_i - \omega_j$ denotes a difference in energies). The rest of the bands (shoulder at higher energies than band (2), not labeled in Fig. 1b) are polarized along the equatorial plane of the nanotubes. By flowing the nanotubes through a cell, they align their long axes with the direction of the flow. Therefore, polarized light parallel to the flow can be used to isolate the transitions to $|I\rangle$ and $|O\rangle$, yielding the simplified absorption spectrum in Fig. 2a.

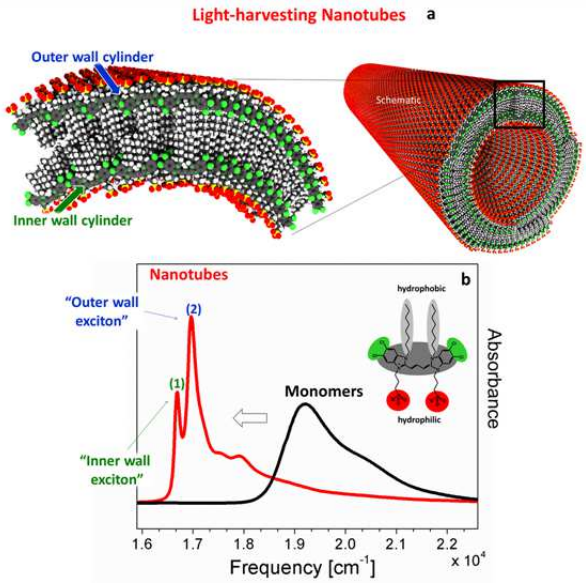

Figure 1: The excitonic system under consideration: Light-harvesting nanotube consisting of a double-walled cylindrical aggregate of amphiphilic cyanine dye molecules. (a) Schematic of the self-assembled light-harvesting nanotube (for clarity using only one molecule per unit cell): double-walled morphology with the hydrophilic sulfonate groups (red) on the exterior, the hydrophobic alkyl chains (light grey) in the interior of the bilayer and the cyanine dye chromophore (dark grey). (b) Absorption spectra of amphiphilic dye monomers C8S3 (black) dissolved in methanol (no aggregation) and nanotubular prepared in water/methanol (red). The nanotube's inner-wall and outer-wall cylinders featuring distinct delocalized exciton bands (1) and band (2) associated with the $|I\rangle$ and $|O\rangle$ excitons. (Reprinted with permission from Eisele, D.M., et al., Nat. Nanotech. (4): 658-663, 2009 and Nat. Chem. (4): 655-662, 2012. Copyright Nature Publishing Group).

The well separated peaks of $|I\rangle$ and $|O\rangle$ (Fig. 1b) suggest a QPT scheme where selectivity is achievable by varying the carrier frequencies of the pulses and fixing their polarizations to be along the long axes of the nanotubes. In particular, we work within a transient grating (TG) setup, where three weak intensity non-collinear narrowband beams with wavectors k_1, k_2, and k_3 interact with the nanotubes, and the coherent signal diffracted at $k_s = -k_1 + k_2 + k_3$ is spectrally interfered with a broadband local oscillator (LO) fourth pulse at $k_4 = k_s$, generating a complex (absorptive and dispersive) spectrum as a function of waiting time $T = t_3 - t_2$ (t_i denotes the arrival time of each pulse) (SI Sec. 2). Pump pulses 1 and 2 interact simultaneously ($t_1 = t_2$) with the sample. The first three narrowband pulses are chosen from a toolbox of two different pulse shapes, namely, a pulse that exclusively excites $|I\rangle$ and another one that excites $|O\rangle$, which we shall label as I and O, respectively. This generates eight different experiments associated with the triads of carrier frequencies: OOO, OOI, III, IIO, OIO, OII, IOI, and IOO. Fig. 2a shows the spectra of the pulses on top of a magnified version of the absorption spectrum of the material from Fig. 1c.

We are interested to probe the dynamics of the SEM. In the TG experiment, the first two pulses prepare an initial SEM state, which then evolves for a waiting time T [13]. The third pulse probes the state at time T by inducing Stimulated Emission (SE) from the SEM to the GSM or Excited State Absorption (ESA) to the Doubly Excited Manifold (DEM). The DEM consists of three states with two excitons each: $|II\rangle$, $|IO\rangle$, and $|OO\rangle$, whose energies we assign as being the sums of the corresponding single-exciton states, with no binding energies, this being a reasonable assumption for molecular excitons (see SI Sec. 4). We also detect the reduced absorption of the third pulse from the ground state $|g\rangle$ (due to the population moved to the SEM), known as Ground State Bleach (GSB). Finally, the decay of this bleach is Ground State Recovery (GSR), which contributes as the population in the SEM decays back to the GSM.

Fig. 2b shows the energy-level diagram for our system, as determined self-consistently from the TG spectra (see SI Sec. 4). The rationale of our QPT scheme is the following (illustrated in Figs. 2c and 3): Narrowband optical pulses allow us to selectively create populations or coherences in the SEM. For instance if $(\omega_1 = \omega_2) = (\omega_{Og}, \omega_{Ig})$, the initial state at the

beginning of the waiting time will be $\rho(0) = |I\rangle\langle O|$ (in the rotating wave approximation (RWA), pulse 1 "acts on the bra" and pulse 2 "acts on the ket" [15, 17]). This state evolves for the waiting time T, when the third pulse and the diffracted probe light can detect it.

Fig. 3 exhaustively enumerates the possible initial states prepared by pulses 1 and 2 and the possible final states detected by pulses 3 and 4, and hence, lists the elements of $\chi(T)$ that are measured by keeping track of each peak in the series of frequency-resolved TG spectra as a function of T. The emission frequencies are associated with the final elements in each Feynman diagram. For instance, let us consider the experiment OIO. Pulses 1 and 2 selectively prepare $|I\rangle\langle O|$, and this state evolves for a time T. There could potentially be nonzero probability amplitudes $\chi_{OOIO}(T)$ and $\chi_{IIIO}(T)$ of population being transferred into $|I\rangle\langle I|$ or $|O\rangle\langle O|$. These processes can be detected with the third pulse O, inducing the SE transition $|O\rangle\langle O| \to |O\rangle\langle g|$ and the ESA transitions $|O\rangle\langle O| \to |OO\rangle\langle O|$, $|I\rangle\langle I| \to |IO\rangle\langle I|$, all of which emit at $\omega_{Og} = \omega_{OO,O} = \omega_{IO,I} = 17068\,\mathrm{cm}^{-1}$ in the corresponding TG spectrum. Similarly, these same elements of $\chi(T)$ contribute to the peak at $\omega_{Ig} = \omega_{II,I} = \omega_{IO,O} = 16635\,\mathrm{cm}^{-1}$ of the experiment OII.

Fig. 4 shows the data obtained from the eight frequency-resolved TG experiments as a function of waiting time T. The data for $T > 500$ fs were not included in the analysis due to the increasing influence of pulse intensity roll-off as a function of delay in our pulse shaping apparatus [37]. The below analysis indicates that the coherent dynamics are complete by 500 fs (see Fig. 5). Both absorptive and dispersive (in our phase convention, real and imaginary, respectively) parts of the complex valued spectra are collected, but we only show the real part. Whereas Fig. 3 predicts that three peaks in frequency domain are possible in each of the spectra, we find surprisingly that there is only one peak of significant amplitude in each spectrum, revealing that nonsecular processes such as coherence to population transfers are negligible or too small to be detected with the current experimental setup. Yet, as noted in the previous paragraph as well as in [9, 12, 13] and SI Sec. 3, some of the peaks report on more than one element of $\chi(T)$, and a more careful procedure to dissect their contributions is necessary. In fact, each peak amplitude can be expressed as a linear combination of elements of $\chi(T)$ where the coefficients are products of transition dipole moments. We extract the required information about the dipoles self-consistently from the TG data via the initial condition $\chi_{ijqp}(0) = \delta_{iq}\delta_{jp}$ (see SI, Sec. 5). The information associated with $\chi(T)$ is then obtained by integrating the area under the complex valued peaks and carrying out a constrained linear inversion procedure. This procedure is a semidefinite programming routine [38, 39] that ensures that the extracted $\chi(T)$ maps physical density matrices as inputs (Hermitian, trace preserving, and positive) to physical density matrices as outputs (SI Sec. 5).

The result of this numerical procedure is in Fig. 5. Table 1 summarizes the values of the elements of $\chi(T)$ together with their timescales given by fits with 95% confidence intervals. The full QPT analysis allows us to conclude that, in this system, as anticipated, the non-secular terms $\chi_{IOOO}(T)$, $\chi_{IOII}(T)$, $\chi_{IOOI}(T)$, $\chi_{IIOI}(T)$, and $\chi_{OOOI}(T)$ are negligible throughout the first 500 fs, indicating weak coupling between populations and coherences, as opposed to the situation of the Fenna-Matthews-Olson complex [40]. On the other hand, $\chi_{OOOO}(T)$ and $\chi_{IIOO}(T)$ indicate that population from the higher $|O\rangle$ state transfers into $|I\rangle$ within 300 fs. The analogous situation with $|I\rangle$ is different. Uphill transfer $|I\rangle \to |O\rangle$ is not observed, $\chi_{OOII}(T) \sim 0$ throughout the experiment, whereas population term $\chi_{IIII}(T) \sim 1$ remains for all the times of interest. Similarly, the explicitly monitored decay terms $\chi_{ggqp}(T)$ are also negligible within that timescale, in consistency with the reported timescales of radiative decay for supramolecular aggregates (on the other of hundreds of picoseconds [41]). Similar conclusions were observed in pump-probe [42] and two-dimensional spectra on the system [43], although maybe using a sample with a different morphology. Finally, we detect electronic coherence between $|O\rangle$ and $|I\rangle$ which lasts for about 150-200 fs, allowing for a few quantum beats to occur before decoherence sets in, indicating that the electronic coupling between the corresponding localized exciton states is weak compared to the coupling of the electronic states to the localized vibrational modes. This coupling was suggested in [43] in the form of weak cross-peaks of the two-dimensional spectra, although quantum beats were not reported there, probably due to a coarser sampling of the waiting time or to peak overlaps. The weak coupling is also consistent with previous redox experiments [36], and its decoherence timescale is similar to reported values on a similar nanotube system with different chemical composition [10, 44–46]. As shown in Table 1, the kinetics of the different processes in this system are characterized by stretched exponentials with indices β ranging between 1.6 and 2. We speculate that this is due to actual exponential kinetics embedded in Gaussian disorder, but more studies are needed to confirm this idea.

Discussion

We have demonstrated for the first time the realization of QPT on a molecular system in condensed phase, namely, the inner and outer wall excitons of a supramolecular light-harvesting nanotube. QPT has been obtained through the collection of a series of frequency-resolved TG spectra by systematically switching the frequency components of the pulses at fixed polarization. Via numerical inversion of these signals, we have reconstructed the full process matrix $\chi(T)$ for the dynamics of the excitons. We summarize the main qualitative findings derived from the analysis of $\chi(T)$. First, an

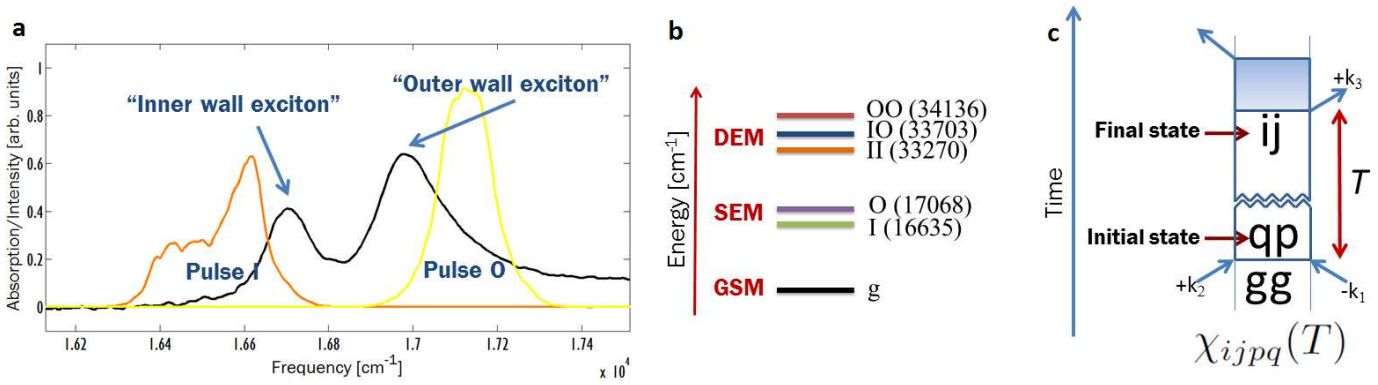

Figure 2: The concepts behind our QPT protocol. (a) Simplified absorption spectrum of the light harvesting nanotubes in the flow cell revealing only two optical transitions when exposed to light that is polarized along the long axes of the nanotubes. Each of the three pulses in each TG experiment is narrowband enough that it is selective towards the $\{|g\rangle \leftrightarrow |I\rangle, |I\rangle \leftrightarrow |II\rangle, |O\rangle \leftrightarrow |IO\rangle\}$ or the $\{|g\rangle \leftrightarrow |O\rangle, |O\rangle \leftrightarrow |OO\rangle, |I\rangle \rightarrow |IO\rangle\}$ transitions, respectively. (b) Energy level diagram of the system. Transitions are allowed between the Ground-State Manifold and any state in the Singly-Excited Manifold, or between any state in the latter and any in the Doubly-Excited Manifold. (c) Double-sided Feynman Diagram representing the general idea of the QPT protocol using TG experiments. The first two pulses prepare the initial state and the last two pulses detect the final state at the end of the waiting time T.

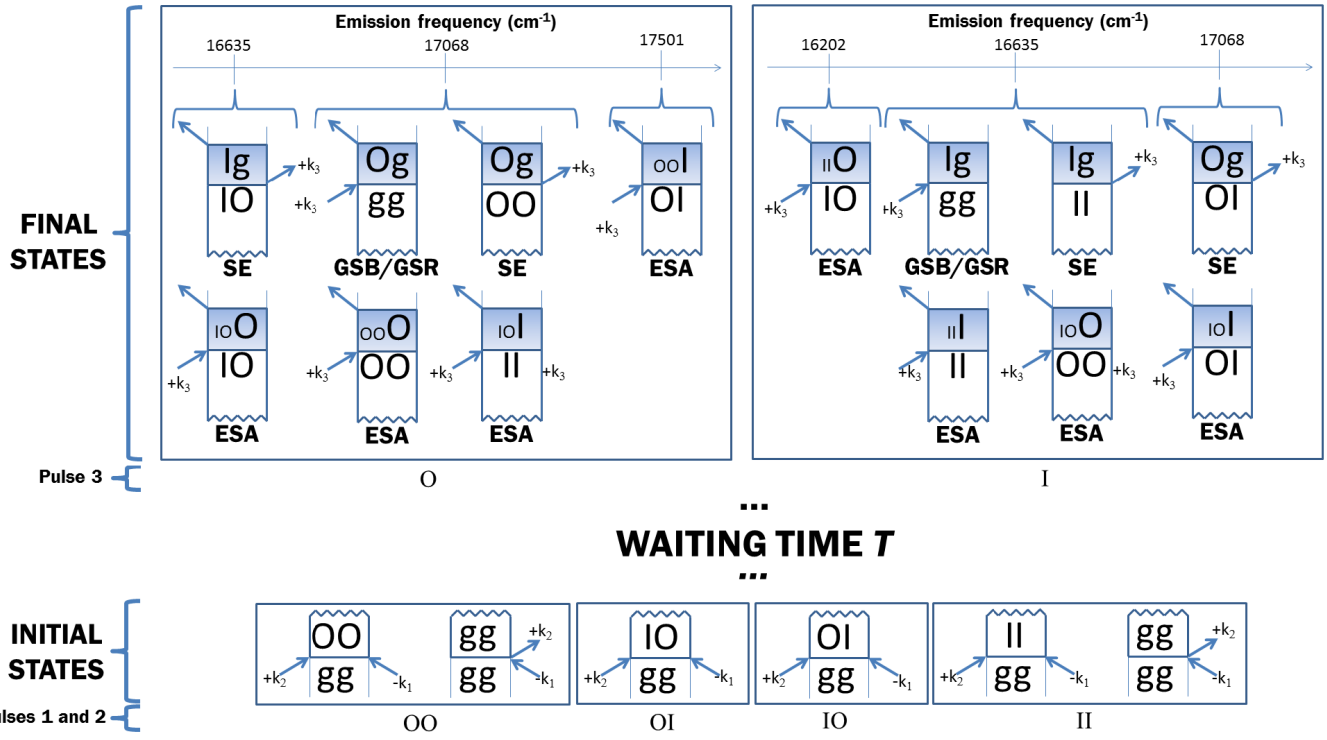

Figure 3: QPT protocol for the two-band exciton system of the double-walled J-aggregate. In the TG setup, the carrier-frequencies of the first two narrowband pulses (bottom) selectively determine the possible initial states. Due to interactions with the vibrational surroundings (the bath), the initial state of the excitons can potentially transfer into other states of the SEM during the waiting time T. Narrowband pulse 3 and broadband LO pulse 4 detect these transfers by producing a frequency-resolved TG spectrum which features a set of emission frequencies that correlate with the state of the system at the end of the waiting time, just as depicted in this figure.

electronic coherence between the inner and outer wall excitons persists for more than a hundred femtoseconds, indicating a weak electronic coupling between the excitons originating from different walls. Second, population transfers quickly from the outer to the inner wall exciton within the first hundreds of femtoseconds, but not the other way around. These transfers deviate from simple exponential kinetics, although this may be an effect of the ensemble measurements. Third, nonsecular relaxation dynamics are measured to be negligible, suggesting that the vibrational bath is dense and Marko-

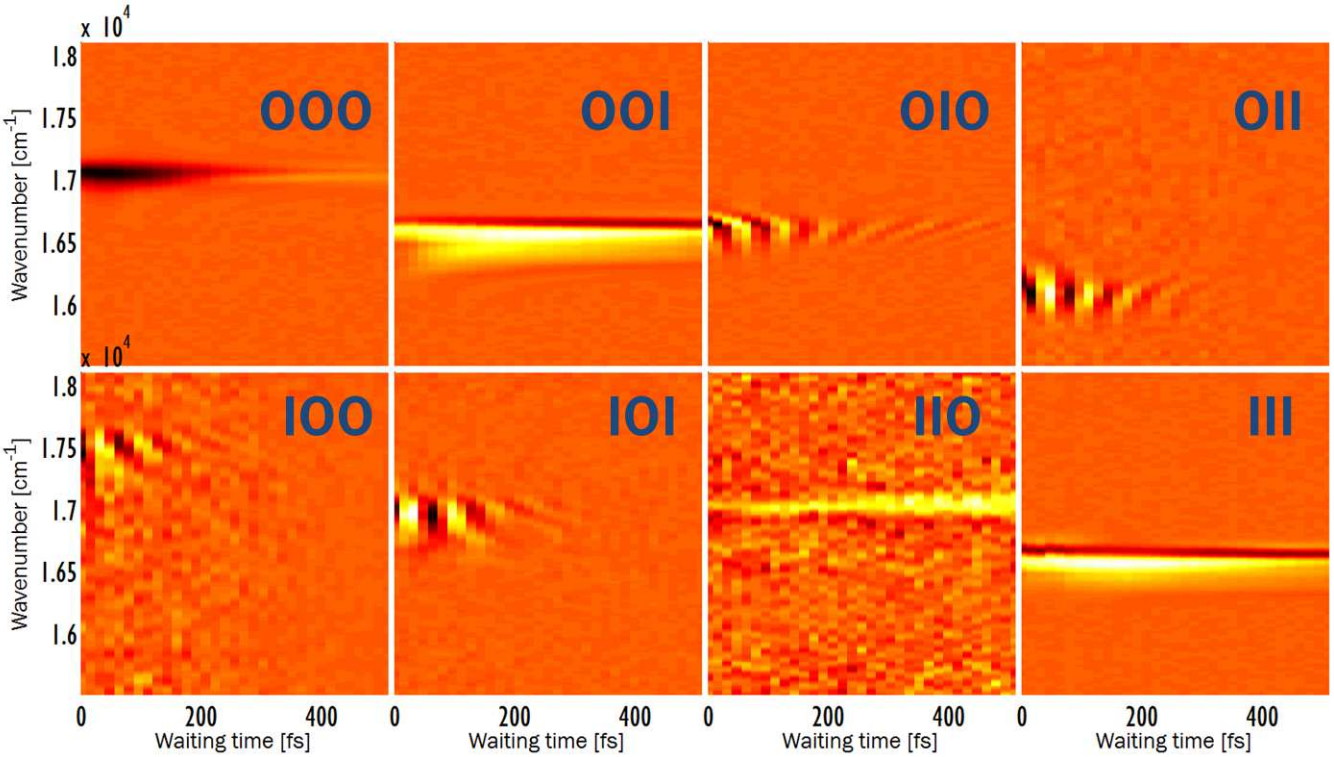

Figure 4: Absorptive part of eight narrowband TG experiments on the two exciton-band system of the double-wall J-aggregate. The data only show one significant peak per spectrum (instead of a maximum of three, as outlined in Fig. 3). Population transfer is revealed in the OOO, OOI, IIO, and III panels, whereas coherence dynamics are monitored by OIO, OII, IOO, and IOI. Coherence between $|I\rangle$ and $|O\rangle$ lasts for about 150 fs at room temperature and observed as fringes as a function of waiting time T. The dispersive part of the data (not shown) exhibits qualitatively similar features.

vian. These conclusions are difficult to assess using a standard broadband approach, where these processes are nontrivially convolved in a few peaks [12]. Instead, our QPT protocol directly isolates each of these contributions in a systematic way.

As we have shown, QPT can be easily carried out by a simple adaptation of the traditional spectroscopic experiment to ensure that the maximum amount of extractable information, at the quantum mechanical level, is obtained. QPT can be interpreted as a procedure that reconstructs the time-dependent quantum state of a system, and therefore, offers a systematic and transparent way to design ultrafast spectroscopy experiments. It complements the traditional approach where only specific projections of the response of the material are collected. Therefore, we envision many opportunities where the QPT paradigm will be powerful. Specific examples include experiments on excitonic networks embedded in complex environments in biological [40] and solid state systems [47], or reactive molecular systems with strong vibronic features [48] where one expects an interesting interplay between electronic coherences and populations beyond secular dynamics, and where the detailed imaging of the quantum dynamics is required in order to construct theoretical models. On the technical side, important directions will be the development of compressed sensing approaches to ameliorate the scaling of QPT as a function of system size [49, 50], or alternatively, partial QPT protocols to pinpoint specific mechanisms that do not require the knowledge of an entire process matrix $\chi(T)$. We foresee exciting opportunities in which the QPT approach to ultrafast spectroscopy will provide new insights into the excited state dynamics of chemical systems.

Acknowledgements

We are grateful for Prof. Marc Baldo's critical reading of the manuscript. All the authors in this work were supported by the Center of Excitonics, an Energy Frontier Research Center funded by the US Department of Energy, Office of Science, Office of Basic Energy Sciences under Award Number DESC0001088. In addition, D.M.E. was partially supported by the Feodor Lynen Research Fellowship from the Alexander von Humboldt-Foundation, J.J.K. was also supported by the Harvard University Center for the Environment and NSERC, and C.P.S. was also supported by an NSF Graduate Research Fellowship.

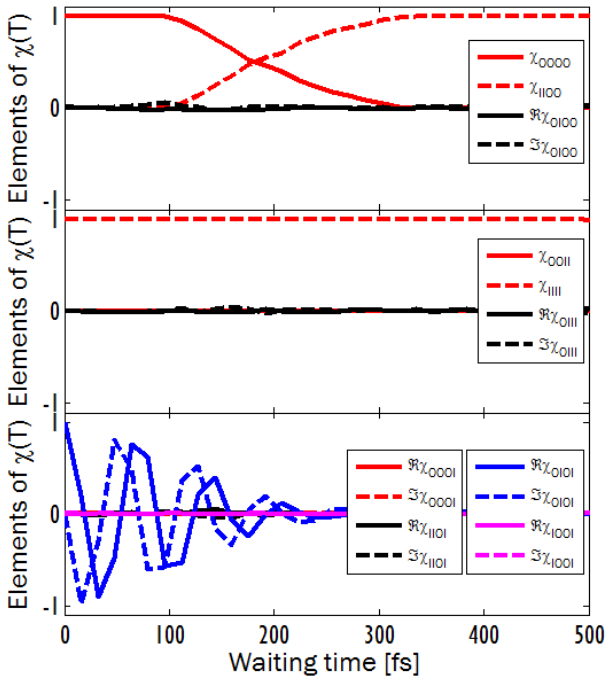

Figure 5: Nonzero elements of $\chi(T)$ extracted from the data of Fig. 4. In the top panel, population transfer from the higher energy $|O\rangle$ to the lower energy $|I\rangle$ is monitored in the decay of $\chi_{OOOO}(T)$ and the rise of $\chi_{IIOO}(T)$ within the first 300 fs. The fall of $\chi_{IIOO}(T)$ is presumably due to subsequent population decay from $|I\rangle$ to $|g\rangle$. In the center panel, the fall from $|I\rangle$ to $|g\rangle$ is observed via $\chi_{IIII}(T)$, although uphill transfer to $|O\rangle$ is not observed from $\chi_{OOII}(T)$. Finally, the right panel shows secular coherence dynamics that last for about 150 fs, which indicates unexpected weak coupling between the I and O states.

Table 1. Summary of timescales of $\chi(T)$

Process	Fit	Description
$\chi_{OOOO}(T) \sim e^{-(T/\tau_{OO})^{\beta_{OO}}}$	$\tau_{OO} = 212 \pm 3\,\text{fs}$, $\beta_{OO} = 3.3 \pm 0.2$.	population decay
$\chi_{IIOO}(T) \sim 1 - e^{-(T/\tau_{OO})^{\beta_{OO}}}$	—	population transfer
$\chi_{IIII}(T) \sim 1\,(> 0.99)$	—	population decay
$\chi_{OOII}(T) \sim 0\,(< 0.01)$	—	population transfer
$\chi_{OIOI}(T) = \chi^*_{IOIO}(T) \sim e^{-i\bar{\omega}_{OI}T} e^{-(T/\tau_{OI})^{\beta_{OI}}}$	$\frac{2\pi}{\omega_{OI}} = 70 \pm 4\,\text{fs}$, $\tau_{OI} = 200 \pm 120\,\text{fs}$, $\beta_{OI} = 2 \pm 1$.	decoherence
$\chi_{IOOO}(T) = \chi^*_{OIOO}(T)$, $\chi_{IOII}(T) = \chi^*_{OIII}(T)$, $\chi_{IOOI}(T) = \chi^*_{OIIO}(T)$, $\chi_{IIOI} = \chi^*_{IIIO}(T)$, $\chi_{OOOI}(T) = \chi^*_{OOIO}(T) < 0.08$	—	nonsecular terms

[1] G. S. Engel, T. R. Calhoun, E. L. Read, T. K. Ahn, T. Mancal, Y. C. Cheng, R. E. Blankenship, and G. R. Fleming. Evidence for wavelike energy transfer through quantum coherence in photosynthetic systems. *Nature*, 446:782–786, 2007.

[2] E. Collini, C. Y. Wong, K. E. Wilk, P. M. G. Curmi, P. Brumer, and G. D. Scholes. Coherently wired light-harvesting in photosynthetic marine algae at ambient temperature. *Nature*, 463:644–U69, 2010.

[3] G. Panitchayangkoon, D. Hayes, K. A. Fransted, J. R. Caram, E. Harel, J. Wen, R. E. Blankenship, and G. S. Engel.

Long-lived quantum coherence in photosynthetic complexes at physiological temperature. *Proc. Natl. Acad. Sci. USA*, 107(29):12766–12770, 2010.

[4] M. Mohseni, P. Rebentrost, S. Lloyd, and A. Aspuru-Guzik. Environment-assisted quantum walks in photosynthetic energy transfer. *J. Chem. Phys.*, 129:174106, 2008.

[5] M. B. Plenio and S. F. Huelga. Dephasing-assisted transport: quantum networks and biomolecules. *New J. Phys.*, 10:113019, 2008.

[6] P. Brumer and M. Shapiro. Molecular response in one-photon absorption via natural thermal light vs. pulsed laser excitation. *Proc. Nat. Acad. Sci.*, 109(48):19575–19578, 2012.

[7] I. Kassal, J. Yuen-Zhou, and S. Rahimi-Keshari. Does coherence enhance transport in photosynthesis? *J. Phys. Chem. Lett.*, 4(3):362–367, 2013.

[8] J. D. Biggs and J. A. Cina. Using wave-packet interferometry to monitor the external vibrational control of electronic excitation transfer. *J. Chem. Phys.*, 131:224101, 2009.

[9] J. Yuen-Zhou, J. J. Krich, and A. Aspuru-Guzik. A witness for coherent electronic vs vibronic-only oscillations in ultrafast spectroscopy. *J. Chem. Phys.*, 136(23):234501, 2012.

[10] F. Milota, V. I. Prokhorenko, T. Mancal, H. von Berlepsch, O. Bixner, H. F. Kauffmann, and J. Hauer. Vibronic and vibrational coherences in two-dimensional electronic spectra of supramolecular j-aggregates. *J. Phys. Chem. A*, 117(29):6007–6014, 2013.

[11] P. Rebentrost, S. Shim, J. Yuen-Zhou, and A. Aspuru-Guzik. Characterization and quantification of the role of coherence in ultrafast quantum biological experiments using quantum master equations, atomistic simulations, and quantum process tomography. *Procedia Chem.*, 3(1):332, 2011.

[12] J. Yuen-Zhou and A. Aspuru-Guzik. Quantum process tomography of excitonic dimers from two-dimensional electronic spectroscopy. i. general theory and application to homodimers. *J. Chem. Phys.*, 134(13):134505, 2011.

[13] Joel Yuen-Zhou, Jacob J. Krich, Masoud Mohseni, and Alán Aspuru-Guzik. Quantum state and process tomography of energy transfer systems via ultrafast spectroscopy. *Proc. Nat. Acad. Sci. USA*, 108(43):17615, 2011.

[14] M. A. Nielsen and I. L. Chuang. *Quantum Computation and Quantum Information*. Cambridge University Press, 2000.

[15] S. Mukamel. *Principles of Nonlinear Optical Spectroscopy*. Oxford University Press, 1995.

[16] S. Mukamel. Multidimensional femtosecond correlation spectroscopies of electronic and vibrational excitations. *Ann. Rev. Phys. Chem.*, 51(1):691–729, 2000.

[17] M. Cho. *Two Dimensional Optical Spectroscopy*. CRC Press, 2009.

[18] M. Riebe, K. Kim, P. Schindler, T. Monz, P. O. Schmidt, T. K. Körber, W. Hänsel, H. Häffner, C. F. Roos, and R. Blatt. Process tomography of ion trap quantum gates. *Phys. Rev. Lett.*, 97:220407, 2006.

[19] A. M. Childs, I. L. Chuang, and D. W. Leung. Realization of quantum process tomography in nmr. *Phys. Rev. A*, 64:012314, 2001.

[20] Y. S. Weinstein, T. F. Havel, J. Emerson, N. Boulant, M. Saraceno, S. Lloyd, and D. G. Cory. Quantum process tomography of the quantum fourier transform. *J. Chem. Phys.*, 121:6117–6133, 2004.

[21] R. C. Bialczak, M. Ansmann, M. Hofheinz, E. Lucero, M. Neeley, A. D. O'Connell, D. Sank, H. Wang, J. Wenner, M. Steffen, A. N. Cleland, and J. M. Martinis. Quantum process tomography of a universal entangling gate implemented with josephson phase qubits. *Nat. Phys.*, 6(6):409–413, 2010.

[22] S. H. Myrskog, J. K. Fox, M. W. Mitchell, and A. M. Steinberg. Quantum process tomography on vibrational states of atoms in an optical lattice. *Phys. Rev. A*, 72:013615, 2005.

[23] M. Howard, J. Twamley, C. Wittmann, T. Gaebel, F. Jelezko, and J. Wrachtrup. Quantum process tomography and linblad estimation of a solid-state qubit. *New J. Phys.*, 8:33, 2006.

[24] M. P. A. Branderhorst, J. Nunn, I. A. Walmsley, and R. L. Kosut. Simplified quantum process tomography. *New J. Phys.*, 11:115010, 2009.

[25] T. S. Humble and J. A. Cina. Molecular state reconstruction by nonlinear wave packet interferometry. *Phys. Rev. Lett.*, 93:060402, 2004.

[26] D. Avisar and D. J. Tannor. Complete reconstruction of the wave function of a reacting molecule by four-wave mixing spectroscopy. *Phys. Rev. Lett.*, 106:170405, 2011.

[27] S. Hoyer, M. Sarovar, and K. B. Whaley. Limits of quantum speedup in photosynthetic light harvesting. *New J. Phys.*, 12(6):065041, 2010.

[28] R. Rey de Castro, R. Cabrera, D. I Bondar, and H. Rabitz. Time-resolved quantum process tomography using hamiltonian-encoding and observable-decoding. *New J. Phys.*, 15(2):025032, 2013.

[29] Umberto De Rossi, Johannes Moll, Monika Spieles, Gunther Bach, Siegfried Dahne, Jorg Kriwanek, and Maria Lisk. Control of the j-aggregation phenomenon by variation of the n-alkyl-substituents. *J. Prak. Chem.-Chem. Ztg.*, 337(1):203–208, 1995.

[30] D. M. Eisele, J. Knoester, S. Kirstein, J. P. Rabe, and D. A. Vanden Bout. Uniform exciton fluorescence from individual molecular nanotubes immobilized on solid substrates. *Nat. Nanotech.*, (4):658–663, 2009.

[31] H. von Berlepsch, S. Kirstein, R. Hania, A. Pugzlys, and C. Bottcher. Modification of the nanoscale structure of the j-aggregate of a sulfonate-substituted amphiphilic carbocyanine dye through incorporation of surface-active additives. *J. Phys. Chem. B*, 111(7):1701–1711, 2007.

[32] D. M. Eisele, H. v. Berlepsch, C. Bottcher, K. J. Stevenson, D. A. Vanden Bout, S. Kirstein, and J. P. Rabe. Photoinitiated growth of sub-7 nm silver nanowires within a chemically active organic nanotubular template. *J. Am. Chem. Soc.*, 132(7):2104–2105, 2010.

[33] A. Olaya-Castro G. D. Scholes, G. R. Fleming and R. van Grondelle. Lessons from nature about solar light harvesting. *Nat. Chem.*, (3):763–774, 2011.

[34] C. Didraga, J. A. Klugkist, and J. Knoester. Optical properties of helical cylindrical molecular aggregates: the homogeneous limit. *J. Phys. Chem. B*, 106:11474–11486, 2002.

[35] C. Didraga, A. Pugzlys, P. R. Hania, H. von Berlepsch, K. Duppen, and J. Knoester. Structure, spectroscopy, and microscopic model of tubular carbocyanine dye aggregates. *J. Phys. Chem. B*, 108(39):14976–14985, 2004.

[36] D. M. Eisele, C. W. Cone, E. A. Bloemsma, S. M. Vlaming, C. G. F. van der Kwaak, R. J. Silbey, M. G. Bawendi, J. Knoester, J. P. Rabe, and D. A. Vanden Bout. Utilizing redox-chemistry to elucidate the nature of exciton transitions in supramolecular dye nanotubes. *Nat. Chem.*, (4):655–662, 2012.

[37] D.B. Turner, Stone K.W., Gundogdu K., and Nelson K.A. The coherent optical laser beam recombination technique (colbert) spectrometer: Coherent multidimensional spectroscopy made easier. *Review of Scientific Instruments*, 82(8):081301, 2011.

[38] M. Grant and S. Boyd. Graph implementations for nonsmooth convex programs. In V. Blondel, S. Boyd, and H. Kimura, editors, *Recent Advances in Learning and Control*, Lecture Notes in Control and Information Sciences, pages 95–110. Springer-

Verlag Limited, 2008.

[39] M. Grant and S. Boyd. Cvx: Matlab software for disciplined convex programming, version 1.21, apr 2011.

[40] G. Panitchayangkoon, D. V. Voronine, D. Abramavicius, J. R. Caram, N. H. C. Lewis, S. Mukamel, and G. S. Engel. Direct evidence of quantum transport in photosynthetic light-harvesting complexes. *Proc. Nat. Acad. Sci. USA*, 108(52):20908–20912, 2011.

[41] J. Moll, S. Daehne, J. R. Durrant, and D. A. Wiersma. Optical dynamics of excitons in j aggregates of a carbocyanine dye. *J. Chem. Phys.*, 102(16):6362–6370, 1995.

[42] R. Augulis, A. Pugzlys, and P. H. M. van Loosdrecht. Exciton dynamics in molecular aggregates. *Phys. Stat. Sol. (c)*, 3(10):3400–3403, 2006.

[43] J. Sperling, A. Nemeth, J. Hauer, D. Abramavicius, S. Mukamel, H. F. Kauffmann, and F. Milota. Excitons and disorder in molecular nanotubes: A 2d electronic spectroscopy study and first comparison to a microscopic model. *J. Phys. Chem. A*, 114(32):8179–8189, 2010.

[44] F. Milota, J. Sperling, A. Nemeth, and H.F. Kauffmann. Two-dimensional electronic photon echoes of a double band j-aggregate: Quantum oscillatory motion versus exciton relaxation. *Chem. Phys.*, 357(1-3):45–53, 2009.

[45] J. M. Womick, S. A. Miller, and A. M. Moran. Probing the dynamics of intraband electronic coherences in cylindrical molecular aggregates. *J. Phys. Chem. A*, 113(24):6587–6598, 2009.

[46] J. M. Womick, S. A. Miller, and A. M. Moran. Correlated exciton fluctuations in cylindrical molecular aggregates. *J. Phys. Chem. B*, 113(19):6630–6639, 2009.

[47] K. W. Stone, K. Gundogdu, D. B. Turner, X. Li, S. T. Cundiff, and K. A. Nelson. Two-quantum 2d ft electronic spectroscopy of biexcitons in gaas quantum wells. *Science*, 324:1169–1173, 2009.

[48] S. Ruetzel, M. Kullmann, J. Buback, P. Nuernberger, and T. Brixner. Tracing the steps of photoinduced chemical reactions in organic molecules by coherent two-dimensional electronic spectroscopy using triggered exchange. *Phys. Rev. Lett.*, 110:148305, Apr 2013.

[49] A. Shabani, R. L. Kosut, M. Mohseni, H. Rabitz, M. A. Broome, M. P. Almeida, A. Fedrizzi, and A. G. White. Efficient measurement of quantum dynamics via compressive sensing. *Phys. Rev. Lett.*, 106(10):100401, 2011.

[50] J. N. Sanders, Semion K. Saikin, S. Mostame, X. Andrade, J. R. Widom, A. H. Marcus, and Alán Aspuru-Guzik. Compressed sensing for multidimensional spectroscopy experiments. *J. Phys. Chem. Lett.*, 3(18):2697–2702, 2012.

Supplementary information

I. SYNTHESIS OF INDIVIDUAL SUPRAMOLECULAR LIGHT-HARVESTING NANOTUBES IN SOLUTION

The amphiphilic cyanine dye derivative 3,3´-bis(2-sulfopropyl)-5,5´,6,6´-tetrachloro-1,1´-dioctylbenzimidacarbocyanine (C8S3, MW=902.8 g mol^{-1}, Fig. 1 in main text) was obtained as a sodium salt (FEW Chemicals) and used as received. The individual supramolecular light-harvesting nanotubes, consisting of concentric walls of excitons, were prepared in water/methanol as described in [1]. Solutions of nanotubes were stored in the dark and used for experiments within four hours. Absorption spectroscopy was used as a tool to monitor the aggregation process before and during the non-linear spectroscopy experiments. We limited our investigation to samples that contained the expected spectral contributions from individual supramolecular light-harvesting nanotubes and had no significant spectral contributions from bundled single-walled light-harvesting nanotubes [2].

II. DESCRIPTION OF OPTICAL SETUP

A non-collinear parametric amplifier [3] (NOPA) is pumped by a regeneratively amplified Ti:sapphire laser at 800 nm with a pulse energy of 350 μJ at a repetition rate of 10 kHz. The NOPA produces pulses with a central frequency of 505 THz, full-width at half-maximum of 21 THz, and approximately equal intensities at 501 and 510 THz, i.e., the energies of the $|I\rangle$ and the $|O\rangle$ states. The pulses are compressed with a prism pair to approximately 20-25 fs.

After the NOPA, the beam passes through a 2D phase mask optimized for first-order diffraction to produce four beams in the BOXCARS geometry. The beams then enter a diffraction-based pulse shaper using a Hamamatsu X7550 2D spatial light modulator (SLM) for phase and amplitude shaping of the frequency components of each beam [4].The beams are spectrally dispersed by a grating and imaged at different vertical positions by a cylindrical lens onto the SLM for independent temporal shaping. We apply a sawtooth grating pattern in the vertical dimension of the SLM device, enabling the amplitude of the frequency components of each beam to be controlled by the amplitude of the grating. In the experiments, a Gaussian amplitude filter is applied via SLM to each beam in order to diffract only the frequencies covering a single transition. Each beam has approximately 3.5 nJ/pulse for the broadband spectrum and 450-500 pJ/pulse for the narrowband spectra.

After pulse shaping, the beams are imaged onto the sample to perform a transient grating experiment. The first two narrowband pulses, with wavevectors k_1 and k_2, generate a spatially periodic excitation grating in the material due to the change in the refractive index upon excitation. The system is probed by the third narrowband pulse after a time delay. The third pulse, with wavevector k_3, diffracts off the grating into the TG direction, $k_s = -k_1 + k_2 + k_3$. The signal co-propagates with the fourth beam, which acts as a (broadband) local oscillator for heterodyne-detection. Spectral interferometry is used to retrieve both the real and imaginary parts of the signal.

This setup is used to obtain 8 different frequency-resolved TG spectra where the first three pulses are narrowband and selective to specific transitions. Between the collection of each TG spectrum, a linear absorption measurement is obtained to ensure that the sample does not degrade.

III. TG EXPERIMENT AS A QPT

The basic idea of carrying out QPT using information from eight different TG spectra collected in the experiment has been intuitively explained in the main text. Here we elaborate on the formal details.

The three pulses interacting with the sample have carrier (center) frequencies $\omega_1, \omega_2, \omega_3$ which are close to the transition energies $\omega_{Ig} = \omega_{II,I} = \omega_{IO,O}$ or $\omega_{Og} = \omega_{OO,O} = \omega_{IO,I}$. We label the first, second, and third pulses as $p, q, r = \mathrm{I}, \mathrm{O}$, respectively, depending on whether they are centered close to ω_{Ig} or ω_{Og}. The pulses generate a third order time-dependent polarization which is detected by the LO pulse (fourth pulse) which, for our purposes, is ideally broadband, covering all the transitions of interest. Under this condition, the complex-valued *frequency-resolved* TG spectrum as a function of waiting time T and frequency ω can be immediately related to the half-sided Fourier transform of the complex-valued TG polarization $P_{k_s}^{pqr}(\tau = 0, T, t)$[13] via,

$$[S_{TG}]^{pqr}(\omega, T) = \int_0^\infty dt e^{i\omega t} P_{k_s}^{pqr}(\tau = 0, T, t). \tag{S1}$$

Here, τ (coherence time) and T (waiting time) correspond to the time intervals between the first and the second, and the second and the third pulses, respectively[14]. The free-induction decay time of the TG polarization is associated with t (sometimes

known as echo-time). Since the half-sided Fourier transform in Eq. (S1) is associated with this time interval, the set of emission frequencies in the TG spectrum $[S_{TG}]^{pqr}(T,\omega)$ corresponds to this free-induction decay. These frequencies are associated with the optical coherences between $|g\rangle$ and the SEM, or between the SEM and the DEM, and they correlate with the detection of different populations and coherences by the end of the waiting time. Consider the scenario where dissipative processes of these optical coherences are not spectrally broader than the separation between the different peaks in the TG spectra, which is what happens in our case. Then, for purposes of QPT, one can properly define the integrated amplitude of the spectra across a specific spectral window of width $2\sigma_4 \equiv 330\,\mathrm{cm}^{-1}$ about the peak centered at a particular frequency ω_4[15],

$$\begin{aligned}[\bar{S}_{TG}]^{pqr}(\omega_4,T) &\equiv \int_{\omega_4-\sigma_4}^{\omega_4+\sigma_4} d\omega [S_{TG}]^{pqr}(\omega,T) \\ &= \int_{-\infty}^{\infty} dt \underbrace{\Theta(t)\sigma_4 \mathrm{sinc}\sigma_4 t e^{i\omega_4 t}}_{\equiv E_4^*(t)} P_{k_s}^{pqr}(\tau=0,T,t), \end{aligned} \tag{S2}$$

where we have used the step function $\Theta(t)$. The interpretation of Eq. (S2) is quite intuitive and reads as follows: Integrating the (broadband LO) *frequency-resolved* complex amplitude $[S_{TG}]^{pqr}(T,\omega)$ across a spectral window $\omega \in [\omega_4-\sigma_4, \omega_4+\sigma_4]$ is equivalent to collecting the total TG photon-count signal arising from the overlap between an *effectively narrowband* LO pulse $E_4(t)$ (with carrier frequency ω_4 and time-width $\sim \sigma_4^{-1}$) centered at the end of the waiting time (at the same time as the third pulse r, at $t=0$) and the t dependent TG polarization $P_{k_s}^{pqr}$ undergoing free-induction decay. ω_4 is chosen to be resonant with one of the emission frequencies. E_4 is short in time (impulsive, broadband), meaning that σ_4 is wide enough to cover the dynamic broadening of a given optical transition. Yet, it is long in time (narrowband) enough to only be selective with respect to the different transitions. In previous articles, we have shown that a TG signal with four "impulsive-yet-selective" pulses prepares and detects populations and coherences in the SEM via the first two and the last two pulses in such a way that the TG experiment may be regarded as a QPT experiment. Hence, from Eq. (S2), we conclude that QPT can also be achieved via the frequency-resolved TG spectra in this article [5, 6].

Fig. 3 in main text shows that the possible emission frequencies, and hence values of ω_4, in the different TG spectra are dictated by the third pulse r. If $r=O$, the induced TG optical coherence and therefore ω_4 take values close to $\omega_{Ig}=\omega_{II,I}=\omega_{IO,O}$ via SE and ESA, at $\omega_{Og}=\omega_{OO,O}=\omega_{IO,I}$ via GSB, SE, ESA, or GSR, or at $\omega_{OO,I}$ via ESA. Similarly, if $r=I$, ω_4 can take values close to $\omega_{II,O}$ via ESA, to $\omega_{Ig}=\omega_{II,I}=\omega_{IO,O}$ via GSB, SE ESA, or GSR, and $\omega_{Og}=\omega_{IO,I}$ via SE or ESA. Hence, for each of the eight frequency-resolved TG spectra $[S_{TG}]^{pqr}(\omega,T)$, there are three possible "carrier frequencies" ω_4 from which we can extract TG signals $[S_{TG}]^{pqr}(\omega_4,T)$, yielding a total of 24 complex numbers as a function of T.

One can readily obtain explicit expressions for $[\bar{S}_{TG}]^{pqr}(\omega_4,T)$ by translating the double-sided Feynman diagrams in Fig. 3 in main text in terms of the initial states prepared by the first two pulses, and the final states detected by the last two pulses [6–8]. If $r=O$, these are,

$$\begin{aligned}[\bar{S}_{TG}]^{pqO}(\omega_4,T) &= C_{pqO} \overbrace{\mu_{pq}\mu_{qg}}^{\text{initial state preparation}} \\ &\times \begin{cases} \overbrace{\mu_{Og}\mu_{Ig}}^{\text{final state detection}} \underbrace{\chi_{IOqp}(T)}_{SE} \underbrace{-\mu_{IO,I}\mu_{IO,O}\chi_{IOqp}(T)}_{ESA} & \text{for } \omega_4=\omega_{Ig}, \\ \underbrace{\mu_{Og}^2\delta_{qp}}_{GSB} \underbrace{-\mu_{Og}^2\chi_{ggqp}(T)}_{GSR} \underbrace{+\mu_{Og}^2\chi_{OOqp}(T)}_{SE} \underbrace{-\mu_{OO,O}^2\chi_{OOqp}(T)}_{ESA} \underbrace{-\mu_{IO,I}^2\chi_{IIqp}(T)}_{ESA} & \text{for } \omega_4=\omega_{Og}, \\ \underbrace{-\mu_{OO,O}\mu_{OO,I}\chi_{OIqp}(T)}_{ESA} & \text{for } \omega_4=\omega_{OO,I}, \end{cases} \end{aligned} \tag{S3}$$

and the analogous expressions hold for $[\bar{S}_{TG}]^{pqI}(\omega_4,T)$ upon the substitutions$O\to I$ and $OO\to II$. Here, we have highlighted the dipole transitions μ_{ij} associated with the initial state preparation and the final state detection in each case. We have also assumed that $\mu_{ij}=\mu_{ji}$ since the excitonic states can be taken to be real due to time-reversal symmetry. For the $\omega_4=\omega_{Og}$ case, it is possible to simplify the expression by assuming that the total exciton population during the waiting time is distributed exclusively among $|O\rangle$, $|I\rangle$, and $|g\rangle$,

$$\chi_{OOqp}(T)+\chi_{IIqp}(T)+\chi_{ggqp}(T)=\delta_{qp}, \tag{S4}$$

so that it reads,

$$[\bar{S}_{TG}]^{pqO}(\omega_4,T) = C_{pqO}\mu_{pg}\mu_{qg}(2\mu_{Og}^2-\mu_{OO,O}^2)\chi_{OOqp}(T)+(\mu_{Og}^2-\mu_{IO,I}^2)\chi_{IIqp}(T) \text{ for } \omega_4=\omega_{Og}. \quad \text{(S5)}$$

This approximation relies on two assumptions: (a) That there are no uphill transfers of population to the DEM during the waiting time, which is very reasonable considering the large energy gap between the SEM and the DEM, and (b) that the transfer to the dark states is also negligible.

C_{pqO} indicates the joint transition probability amplitude to carry out the three different dipole transitions via the three different pulses. Whereas in principle one can obtain explicit expressions for this amplitude, in the present case, the narrowband pulses with imperfect Gaussian forms, the pulse overlaps, as well as the broadening of the TG transitions due to dynamic disorder altogether impede its precise determination. We shall write it as,

$$\begin{aligned} C_{pqO} &= f_{pq}E_p(\omega_{pg})E_q(\omega_{qg})E_O(\omega_{Og}) \\ &\approx f_{pq}\max(E_p(\omega))\max(E_q(\omega))\max(E_O(\omega)). \end{aligned} \quad \text{(S6)}$$

Here, we have used the fact that the pulses are narrowband and centered about the relevant transitions ($E_p(\omega_{pq}) \approx \max(E_p(\omega))$ and so on), and we extract the respective amplitudes from the power spectra of the pulses, $E_i(\omega) = \sqrt{|E_i(\omega)|^2}$ (assuming $E_i(\omega)$ has no chirp and its global phase is already considered in the phasing procedure with respect to the other pulses). We hide all the complexity of C_{pqO} in the complex-valued factor f_{pq} which takes into account the overlap between pulses p and q. Finally, from the absorption spectrum, we can get a good estimate of

$$\frac{\mu_{Og}}{\mu_{Ig}} \approx \sqrt{\frac{A(\omega_{Og})}{A(\omega_{Ig})}}, \quad \text{(S7)}$$

where $A(\omega)$ is the absorption spectrum of the material. Note that the contributions corresponding to SE/GSB and ESA/GSR involve a net gain and loss of photons to the electric field in the k_s direction, respectively, and hence come with opposite signs. Also, GSB appears only if the first two pulses are resonant with the same transitions and therefore create a population (rather than a coherence) in the excited state, and hence, it is proportional to δ_{pq}. Since the GSB term monitors (stationary) ground state population during the waiting time T, it is proportional to $\chi_{gggg}(T)=1$ and shows up as a T-independent background[16].

So far, we have 24 effective narrowband time (or frequency) integrated complex-valued TG signals $[S_{TG}]^{pqr}(T,\omega)$ which amount to 48 real-valued data points as a function of T. Note that in general, these signals are linear combinations of different elements of $\chi(T)$ and, in fact, according to Eq. (S3), several signals report on a single element of $\chi(T)$ at a time. Let us now count the number of elements of $\chi(T)$ to invert for our two-level system composed of $|I\rangle$ and $|O\rangle$. Hermicity of $\chi(T)$ requires that $\chi_{ijqp}(T) = \chi^*_{jipq}(T)$. This amounts to the real-valued population terms $\chi_{OOOO}(T)$, $\chi_{IIOO}(T)$, $\chi_{IIII}(T)$, and $\chi_{OOII}(T)$, and the complex-valued $\chi_{IOIO}(T) = \chi^*_{OIOI}(T)$, together with the non-secular (not energy conserving, also complex-valued) terms $\chi_{IOOO}(T) = \chi^*_{OIOO}(T)$, $\chi_{IOII}(T) = \chi_{IOII}(T)$, $\chi_{IOOI}(T) = \chi^*_{OIIO}(T)$, $\chi_{OOIO}(T) = \chi^*_{OOOI}(T)$, and $\chi_{IIIO}(T) = \chi^*_{IIOI}(T)$. Based on this symmetry, there are 16 real parameters of $\chi(T)$ to extract [17] out of a redundant set of 48 real-valued data points.

IV. ENERGY LEVEL ASSIGNMENTS

Energies of the SEM and DEM states addressed in our experiment have been self-consistently assigned from the frequency-resolved TG spectra. As a first examination, from the linear absorption, peak maxima corresponding to $|I\rangle$ and $|O\rangle$ are located at $\omega_{Ig} = 16695\,\mathrm{cm}^{-1}$ and $\omega_{Og} = 16970\,\mathrm{cm}^{-1}$, respectively. These peaks are broadened both by static and dynamic disorder of the ensemble. As shown in Fig. 2 in main text, narrowband excitation in the experiment is effected in such a way that the pulses are centered at the edge of each band, therefore selecting only a subset of realizations of static disorder. Therefore, the average energies in the linear absorption do not coincide with those probed in the TG experiment. Hence, it is more accurate to extract the energy levels of interest from the TG spectra themselves using the initial condition

$$\chi_{ijqp}(0) = \delta_{iq}\delta_{jp}, \quad \text{(S8)}$$

For instance, whereas the OOO spectrum can potentially contain three different emission frequencies, at $T=0$ it consists of a single peak[18] with maximum amplitude at $\omega \sim 17068\,\mathrm{cm}^{-1}$. This peak must correspond to (see Eq. (S3); also Fig. 3 in main text, left top panel) $\chi_{OOOO}(0)=1$, in a combination of SE, ESA, and GSB processes. Whereas SE/GSB is expected to show up at $\sim$3.5 cm^{-1} red-shifted from ESA at cryogenic temperatures [9], dynamic and some static disorder at room temperature forbids an unambiguous discrimination as it broadens peaks up to a total width of about 330 cm^{-1}, as mentioned at the beginning of SI, Sec. III. From here, we infer that $\omega_{Og}, \omega_{OO,O} \sim 17068\,\mathrm{cm}^{-1}$. Analogously, from the III spectrum at $T=0$ and $\chi_{IIII}(0)=1$, we obtain $\omega_{Ig}, \omega_{II,I} \sim 16635\,\mathrm{cm}^{-1}$. Based on these observations, we use $\omega_{Og} = \omega_{OO,O} = 17068\,\mathrm{cm}^{-1}$ and $\omega_{Ig} = \omega_{II,I} = 16635\,\mathrm{cm}^{-1}$.

The presence of the SEM states $|I\rangle$ and $|O\rangle$ demand the consideration of an additional combination exciton $|IO\rangle$, which we treat as a doubly-excited state where the two excitons are present, one in $|I\rangle$ and the other in $|O\rangle$, and its energy is the sum of the two SEM exciton energies, $\omega_{IO,O} = \omega_{Ig}$ and $\omega_{IO,I} = \omega_{Og}$. This is a reasonable assumption considering that the interactions between the $|I\rangle$ and the $|O\rangle$ excitons will be weak across the 4 nm hydrophobic core separating them.

We confirm the extracted energies by analyzing the rest of the TG spectra at $T = 0$. First, OOI and IIO spectra each contain a single peak at 16572 and 17025 cm^{-1}, respectively. Due to the frequencies of the pulses involved in these two experiments, only GSB and ESA processes contribute at $\omega = \omega_{Ig} = \omega_{IO,O}$ and $\omega = \omega_{Og} = \omega_{IO,I}$, which is to a good approximation what we see. Second, spectra IOI and OIO show peaks at 17012 and 16635 cm^{-1}, associated with SE and ESA at $\omega = \omega_{Og} = \omega_{IO,I}$ and $\omega = \omega_{Ig} = \omega_{IO,O}$. Finally, IOO and OII spectra show peaks at 17452 and 16118 cm^{-1} corresponding to ESA at $\omega = \omega_{OO,I}$ and $\omega = \omega_{II,O}$. These observations validate the energy assignments in Fig. 2b in main text.

V. DATA PROCESSING

As explained in SI Sec. III, Fig. 3 in main text and Eq. (S3) comprehensively enumerate the possible processes within the SEM that can be detected from the eight different TG spectra beyond $T = 0$. In principle, they manifest as three spectrally well-separated peaks in each TG spectrum, indicating general transfers amongst populations and coherences.

For each of the possible TG emission frequencies ω_4, we have computed the integral of the raw complex spectra given by Eq. (S2) using a half-width of $\sigma_4 = 165\,\text{cm}^{-1}$. Since the centers of the bands are separated farther than 330 cm^{-1} from one another, the TG emission bands are very well-separated. The obtained set of signals is quite sparse. Table S1 shows the normalized contribution of $\sum_T |[\bar{S}_{TG}]^{pqr}(\omega_4, T)|^2$ for each frequency-resolved TG spectrum. Together with each entry, we have also indicated the element of $\chi(T)$ associated with each signal. For instance, the peak centered at $\omega_{Og} = \omega_{OO,O}$ in the IIO spectra reports on both $\chi_{OOII}(T)$ and $\chi_{IIII}(T)$, whereas the peak at $\omega_{II,O}$ in OII is directly proportional to χ_{IOIO}. To obtain a rough idea of the experimental data, we have highlighted the entries that contribute the most per TG spectrum, and most of them account for over 97% of the total norm of the respective experiment, yielding what looks like a sparse data set.

TABLE S1. Normalized contribution of $\sum_T |[\bar{S}_{TG}]^{pqr}(\omega_4, T)|^2$

TG spectrum\ω_4 [cm^{-1}]	$\omega_{Ig} = 16635\,\text{cm}^{-1}$	$\omega_{Og} = \omega_{OO,O} = \omega_{IO,I} = 17068\,\text{cm}^{-1}$	$\omega_{OO,I} = 17501\,\text{cm}^{-1}$
OOO	0.0001 (χ_{IOOO})	**0.9999** (χ_{OOOO}, χ_{IIOO})	0.0000 (χ_{OIOO})
IIO	0.0622 (χ_{IOII})	**0.9007** (χ_{OOII}, χ_{IIII})	0.0371 (χ_{OIII})
IOO	0.0320 (χ_{IOOI})	0.1231 (χ_{OOOI}, χ_{IIOI})	**0.8449** (χ_{OIOI})
OIO	**0.9973** (χ_{IOIO})	0.0018 (χ_{OOIO}, χ_{IIIO})	0.0009 (χ_{OIIO})
TG spectrum\ω_4 [cm^{-1}]	$\omega_{II,O} = 16202\,\text{cm}^{-1}$	$\omega_{Ig} = \omega_{II,I} = \omega_{IO,O} = 16635\,\text{cm}^{-1}$	$\omega_{Og} = 17068\,\text{cm}^{-1}$
OOI	0.0221 (χ_{IOOO})	**0.9779** (χ_{OOOO}, χ_{IIOO})	0.0000 (χ_{OIOO})
III	0.0050 (χ_{IOII})	**0.9947** (χ_{OOII}, χ_{IIII})	0.0003 (χ_{OIII})
IOI	0.0018 (χ_{IOOI})	0.0689 (χ_{IIOI}, χ_{OOOI})	**0.9294** (χ_{OIOI})
OII	**0.9886** (χ_{IOIO})	0.0061 (χ_{IIIO}, χ_{OOIO})	0.0052 (χ_{OIIO})

Note that the entries with small contributions correspond to nonsecular terms. Whereas this table serves as an illustration to the rationale behind our procedure, we do not use it for the numerics *per se*, as the signals do not correspond to the elements of $\chi(T)$ alone, but are weighed by dipole moment and electric field terms. To proceed in a more systematic fashion, we follow the following procedure:

1. From each signal $[\bar{S}_{TG}]^{pqr}(\omega_4, T)$ in Eq. (S3), construct

$$[\bar{s}_{TG}]^{pqr}(\omega_4, T) = \frac{[\bar{S}_{TG}]^{pqr}(\omega_4, T)}{\max(E_p(\omega))\max(E_q(\omega))\max(E_r(\omega))\mu_{pq}\mu_{gq}}, \tag{S9}$$

   where the dipoles are given in units of μ_{Ig} (using Eq. (S7)).

2. Taking into account the initial condition Eq. (S8) in Eqs. (S9) and (S5) as well as their analogues upon the $O \to I$ and $OO \to II$ substitutions, yields the following coefficients,

$$
\begin{aligned}
A &\equiv [\bar{s}_{TG}]^{OOO}(\omega_{Og},0) = f_{OO}(2\mu_{Og}^2 - \mu_{OO,O}^2),\\
B &\equiv [\bar{s}_{TG}]^{IIO}(\omega_{Og},0) = f_{II}(\mu_{Og}^2 - \mu_{IO,I}^2),\\
C &\equiv [\bar{s}_{TG}]^{OOI}(\omega_{Ig},0) = f_{OO}(\mu_{Ig}^2 - \mu_{IO,O}^2),\\
D &\equiv [\bar{s}_{TG}]^{III}(\omega_{Ig},0) = f_{II}(2\mu_{Ig}^2 - \mu_{II,I}^2),\\
E &\equiv [\bar{s}_{TG}]^{IOI}(\omega_{Og},0) = f_{IO}(\mu_{Ig}\mu_{Og} - \mu_{IO,I}\mu_{IO,O}),\\
F &\equiv [\bar{s}_{TG}]^{IOO}(\omega_{OO,I},0) = f_{IO}(\mu_{OO,O}\mu_{OO,I}),\\
G &\equiv [\bar{s}_{TG}]^{OIO}(\omega_{Ig},0) = f_{OI}(\mu_{Og}\mu_{Ig} - \mu_{IO,O}\mu_{IO,I}).\\
H &\equiv [\bar{s}_{TG}]^{OII}(\omega_{II,O},0) = f_{OI}(\mu_{II,I}\mu_{II,O}).
\end{aligned}
\tag{S10}
$$

These coefficients precisely constitute the set of dipole combinations required for the inversion of $\chi(T)$ from Eq. (S3)).

3. In order to make use of linear algebra, the coefficients from Eq. (S10) are arranged into matrices,

$$
\underline{\mathbb{M}}_{OO} = \underline{\mathbb{M}}_{II} \equiv \begin{bmatrix} 0 & 0 & G & -iG \\ A & B & 0 & 0 \\ 0 & 0 & F & iF \\ 0 & 0 & H & -iH \\ C & D & 0 & 0 \\ 0 & 0 & E & iE \end{bmatrix}, \underline{\mathbb{M}}_{OI} \equiv \begin{bmatrix} 0 & 0 & G & 0 & 0 & 0 & -iG & 0 \\ A & B & 0 & 0 & -iA & -iB & 0 & 0 \\ 0 & 0 & 0 & F & 0 & 0 & 0 & -iF \\ 0 & 0 & H & 0 & 0 & 0 & -iH & 0 \\ C & D & 0 & 0 & -iC & -iD & 0 & 0 \\ 0 & 0 & 0 & E & 0 & 0 & 0 & -iE \\ 0 & 0 & 0 & G & 0 & 0 & 0 & iG \\ A & B & 0 & 0 & iA & iB & 0 & 0 \\ 0 & 0 & F & 0 & 0 & 0 & iF & 0 \\ 0 & 0 & 0 & H & 0 & 0 & 0 & iH \\ C & D & 0 & 0 & iC & iD & 0 & 0 \\ 0 & 0 & E & 0 & 0 & 0 & iE & 0 \end{bmatrix},
\tag{S11}
$$

whereas the signals are organized as vectors,

$$
\mathbb{S}_{OO}(T) = \begin{bmatrix} [\bar{s}_{TG}]^{OOO}(\omega_{Ig},T) \\ [\bar{s}_{TG}]^{OOO}(\omega_{Og},T) \\ [\bar{s}_{TG}]^{OOO}(\omega_{OO,I},T) \\ [\bar{s}_{TG}]^{OOI}(\omega_{II,O},T) \\ [\bar{s}_{TG}]^{OOI}(\omega_{Ig},T) \\ [\bar{s}_{TG}]^{OOI}(\omega_{Og},T) \end{bmatrix}, \mathbb{S}_{II}(T) = \begin{bmatrix} [\bar{s}_{TG}]^{IIO}(\omega_{Ig},T) \\ [\bar{s}_{TG}]^{IIO}(\omega_{Og},T) \\ [\bar{s}_{TG}]^{IIO}(\omega_{OO,I},T) \\ [\bar{s}_{TG}]^{III}(\omega_{II,O},T) \\ [\bar{s}_{TG}]^{III}(\omega_{Ig},T) \\ [\bar{s}_{TG}]^{III}(\omega_{Og},T) \end{bmatrix}, \mathbb{S}_{OI}(T) = \begin{bmatrix} [\bar{s}_{TG}]^{OIO}(\omega_{Ig},T) \\ [\bar{s}_{TG}]^{OIO}(\omega_{Og},T) \\ [\bar{s}_{TG}]^{OIO}(\omega_{OO,I},T) \\ [\bar{s}_{TG}]^{OII}(\omega_{II,O},T) \\ [\bar{s}_{TG}]^{OII}(\omega_{Ig},T) \\ [\bar{s}_{TG}]^{OII}(\omega_{Og},T) \\ [\bar{s}_{TG}]^{IOO}(\omega_{Ig},T) \\ [\bar{s}_{TG}]^{IOO}(\omega_{Og},T) \\ [\bar{s}_{TG}]^{IOO}(\omega_{OO,I},T) \\ [\bar{s}_{TG}]^{IOI}(\omega_{II,O},T) \\ [\bar{s}_{TG}]^{IOI}(\omega_{Ig},T) \\ [\bar{s}_{TG}]^{IOI}(\omega_{Og},T) \end{bmatrix}.
\tag{S12}
$$

The goal is to extract $\chi(T)$, which is also written as a series of vectors,

$$\mathbb{X}_{OO}(T) \equiv \begin{bmatrix} \chi_{OOOO}(T) \\ \chi_{IIOO}(T) \\ \Re\{\chi_{OIOO}(T)\} \\ \Im\{\chi_{OIOO}(T)\} \end{bmatrix}, \mathbb{X}_{II}(T) \equiv \begin{bmatrix} \chi_{OOII}(T) \\ \chi_{IIII}(T) \\ \Re\{\chi_{OIII}(T)\} \\ \Im\{\chi_{OIII}(T)\} \end{bmatrix}, \mathbb{X}_{OI}(T) = \begin{bmatrix} \Re\{\chi_{OOOI}\} \\ \Re\{\chi_{IIOI}\} \\ \Re\{\chi_{OIOI}\} \\ \Re\{\chi_{IOOI}\} \\ \Im\{\chi_{OOOI}\} \\ \Im\{\chi_{IIOI}\} \\ \Im\{\chi_{OIOI}\} \\ \Im\{\chi_{IOOI}\} \end{bmatrix},$$

which fulfill,

$$\begin{aligned} \underline{\mathbb{M}}_{OO}\mathbb{X}_{OO}(T) &= \mathbb{S}_{OO}(T), \\ \underline{\mathbb{M}}_{II}\mathbb{X}_{II}(T) &= \mathbb{S}_{II}(T), \\ \underline{\mathbb{M}}_{OI}\mathbb{X}_{OI}(T) &= \mathbb{S}_{OI}(T). \end{aligned} \tag{S13}$$

Clearly, Eq. (S13) can be written as a single matrix equation $\underline{\mathbb{M}}\mathbb{X}(T) = \mathbb{S}(T)$, where $\underline{\mathbb{M}} = \underline{\mathbb{M}}_{OO} \bigoplus \underline{\mathbb{M}}_{II} \bigoplus \underline{\mathbb{M}}_{OI}$ is a 24×16 matrix with each of the original matrices along the diagonal and zeros for the rest of the entries, i.e., it is of the block-diagonal form. $\mathbb{X}(T)$ and $\mathbb{S}(T)$ are the concatenations of the corresponding column vectors and have sizes 16 and 24, respectively. The condition number of $\underline{\mathbb{M}}$ is equal to 14.9, which indicates a well-behaved inversion, associated with the sparsity of the matrix[19]. Yet a naive direct inversion of $\underline{\mathbb{M}}$ yields unphysical values of the process matrix $\chi(T)$ (in this case, of the vector $\mathbb{X}(T)$) in general. Via a semidefinite programming routine built using the CVX software [10, 11], we impose the positive-semidefinite constraint,

$$\sum_{ijqp} z^*_{iq} \chi_{ijqp}(T) z_{jp} \geq 0, \tag{S14}$$

for any complex-valued matrix z. This condition guarantees that the inverted $\chi(T)$ maps positive density matrices to other positive density matrices. The result of this numerical procedure is given in Fig. 5 in main text, where most of the elements of $\chi(T)$ (namely, the nonsecular terms) result to be negligible.

4. Since we do not precisely know the dipoles of the system, we now test the sensitivity of the extracted $\chi(T)$ to the dipole coefficients $\underline{\mathbb{M}}$ (Eq. (S11)). We modify $\underline{\mathbb{M}}$ by scaling one of the coefficients by a factor and keeping the rest fixed. This generates a matrix $\underline{\mathbb{M}}'$ from which we can extract a new $\mathbb{X}'(T)$. We compute two error measures associated with this perturbation,

$$\text{Error}_1(\underline{\mathbb{M}}') = \frac{\max_{ijqp} \sum_T |\chi_{ijqp}(T) - \chi'_{ijqp}(T)|}{\text{Number of } T\text{points}}, \tag{S15}$$

$$\text{Error}_2(\underline{\mathbb{M}}') = \frac{\max_T \sum_{ijqp} |\chi_{ijqp}(T) - \chi'_{ijqp}(T)|}{\text{Number of elements in } \mathbb{X}(\text{T})}, \tag{S16}$$

where the Number of Tpoints is 33 (from 0 to 510 fs) and the Number of elements in $\mathbb{X}$(T) is 16 (the size of $\mathbb{X}(T)$). The results of these calculations are shown in Table S2-1 and 2. Notice that $\text{Error}_2(\underline{\mathbb{M}}')$ is in general smaller than $\text{Error}_1(\underline{\mathbb{M}}')$. This has to do with the fact that most of the elements of $\chi(T)$, the nonsecular terms, are negligible, and varying the coefficients of $\underline{\mathbb{M}}$ keeps them that way, which is a good sign. Since $\text{Error}_2(\underline{\mathbb{M}}')$ averages the error over the different elements of $\chi(T)$, the nonsecular terms "buffer" the errors from the other terms. On the other hand, $\text{Error}_1(\underline{\mathbb{M}}')$ averages instead over the T points, and singles out the highest deviation amongst the different elements of $\chi(T)$.

Table S2-1 shows that our extracted process matrices are most sensitive to deviations in the coefficient D. In particular, scaling D by a factor of -1.6, -4 or ± 10 can cause significant deviations in at least one element of $\chi(T)$. Multiplying D

by a factor of 1.6 does not cause large changes in $\chi(T)$. In evaluating D, we assume that $\mu_{II,I} = \mu_{Ig}$. This approximation could be checked by quantum chemistry calculations. The other dipole combinations must be wrong by at least a factor of ± 10 before significant errors in $\chi(T)$ are introduced. And the results seem largely independent of the value of F entirely. These observations, together with the relatively small condition number of $\mathbb{M}$, indicate that the inversion of $\mathbb{X}(T)$, and hence the QPT, is not too sensitive to the precise values of the coefficients of $\mathbb{M}$.

TABLE S2-1. Sensitivity analysis of errors on the coefficients of $\mathbb{M}$ (Error_1)

Coefficient\Scaling factor	**-10**	**-4**	**-1.6**	**-0.6**	**-0.25**	**-0.1**	**0.1**	**0.25**	**0.6**	**1**	**1.6**	**4**	**10**
A	0.38	0.39	0.39	0.36	0.21	0.13	0.06	0.09	0.06	0	0.12	0.28	0.34
B	0.81	0.14	0.01	0.01	0.01	0.01	0	0	0	0	0.01	0.16	0.79
C	0.37	0.15	0.07	0.04	0.03	0.02	0.02	0.01	0.01	0	0.01	0.09	0.32
D	0.99	0.98	0.9	0.81	0.77	0.68	0.24	0.02	0.01	0	0.21	0.67	0.87
E	0.21	0.23	0.03	0.05	0.07	0.07	0.07	0.07	0.06	0	0.03	0.15	0.18
F	0.04	0.02	0.01	0.01	0.01	0.01	0.01	0.01	0.01	0	0.01	0.02	0.04
G	0.22	0.26	0.37	0.06	0.06	0.06	0.05	0.04	0.02	0	0.05	0.12	0.16
H	0.21	0.23	0.05	0.03	0.07	0.07	0.07	0.07	0.05	0	0.03	0.15	0.18

TABLE S2-2. Sensitivity analysis of errors on the coefficients of $\mathbb{M}$ (Error_2)

Coefficient\Scaling factor	**-10**	**-4**	**-1.6**	**-0.6**	**-0.25**	**-0.1**	**0.1**	**0.25**	**0.6**	**1**	**1.6**	**4**	**10**
A	0.2	0.2	0.19	0.17	0.1	0.1	0.06	0.06	0.04	0	0.05	0.13	0.17
B	0.13	0.04	0.01	0.01	0.01	0.01	0.01	0.01	0	0	0	0.03	0.08
C	0.19	0.07	0.03	0.01	0.01	0.01	0.01	0.01	0	0	0.01	0.05	0.14
D	0.14	0.13	0.13	0.13	0.13	0.07	0.04	0.01	0.01	0	0.04	0.09	0.11
E	0.09	0.11	0.02	0.03	0.04	0.05	0.05	0.05	0.03	0	0.02	0.07	0.08
F	0.02	0.01	0.01	0	0.01	0.01	0.01	0.01	0	0	0.01	0.01	0.02
G	0.1	0.11	0.16	0.04	0.03	0.03	0.03	0.02	0.02	0	0.03	0.06	0.07
H	0.1	0.11	0.03	0.02	0.04	0.04	0.05	0.05	0.03	0	0.02	0.08	0.08

[1] D. M. Eisele, J. Knoester, S. Kirstein, J. P. Rabe, and D. A. Vanden Bout. Uniform exciton fluorescence from individual molecular nanotubes immobilized on solid substrates. *Nat. Nanotech.*, (4):658–663, 2009.

[2] D. M. Eisele, C. W. Cone, E. A. Bloemsma, S. M. Vlaming, C. G. F. van der Kwaak, R. J. Silbey, M. G. Bawendi, J. Knoester, J. P. Rabe, and D. A. Vanden Bout. Utilizing redox-chemistry to elucidate the nature of exciton transitions in supramolecular dye nanotubes. *Nat. Chem.*, (4):655–662, 2012.

[3] G. Cerullo and S. De Silvestri. Ultrafast optical parametric amplifiers. *Rev. Sci. Instrum.*, 74(1):1–18, 2003.

[4] D.B. Turner, Stone K.W., Gundogdu K., and Nelson K.A. The coherent optical laser beam recombination technique (colbert) spectrometer: Coherent multidimensional spectroscopy made easier. *Review of Scientific Instruments*, 82(8):081301, 2011.

[5] J. Yuen-Zhou and A. Aspuru-Guzik. Quantum process tomography of excitonic dimers from two-dimensional electronic spectroscopy. i. general theory and application to homodimers. *J. Chem. Phys.*, 134(13):134505, 2011.

[6] Joel Yuen-Zhou, Jacob J. Krich, Masoud Mohseni, and Alán Aspuru-Guzik. Quantum state and process tomography of energy transfer systems via ultrafast spectroscopy. *Proc. Nat. Acad. Sci. USA*, 108(43):17615, 2011.

[7] J. Yuen-Zhou, J. J. Krich, and A. Aspuru-Guzik. A witness for coherent electronic vs vibronic-only oscillations in ultrafast spectroscopy. *J. Chem. Phys.*, 136(23):234501, 2012.

[8] J. Yuen-Zhou, J. J. Krich, I. Kassal, and A. Aspuru-Guzik. *Ultrafast Dynamics in Biomolecular Systems*, chapter Ultrafast Spectroscopy: Wavepackets and Quantum Information, page 1. PanStanford, Singapore, 2013.

[9] R. Augulis, A. Pugzlys, and P. H. M. van Loosdrecht. Exciton dynamics in molecular aggregates. *Phys. Stat. Sol. (c)*, 3(10):3400–3403, 2006.

[10] M. Grant and S. Boyd. Graph implementations for nonsmooth convex programs. In V. Blondel, S. Boyd, and H. Kimura, editors, *Recent Advances in Learning and Control*, Lecture Notes in Control and Information Sciences, pages 95–110. Springer-Verlag Limited, 2008.

[11] M. Grant and S. Boyd. Cvx: Matlab software for disciplined convex programming, version 1.21, apr 2011.

[12] U. Banin, A. Bartana, S. Ruhman, and R. Kosloff. Impulsive excitation of coherent vibrational motion ground surface dynamics induced by intense short pulses. *J. Chem. Phys.*, 101(10):8461–8481, 1994.

[13] More precisely, the scalar $P_{k_s}^{pqr}$ is the projection of the TG polarization on the LO field, which is parallel to the axes of the nanotubes (as are the other pulses). Note the dual use of the word *polarization.* Here, it refers to the electric dipole density in the material, but we also use it to denote the direction of the electric field of the pulses.

[14] When $\tau \neq 0$, the TG experiment generalizes to the photon-echo configuration, which for our QPT purposes is not necessary.

[15] The peaks are separated from one another by $\sim$330 cm^{-1} so windows of width 330 cm^{-1} are sufficiently narrow to detect single peak contributions, and broad enough to contain all the relevant spectral diffusion.

[16] This is not true if the pump pulses 1 and 2 prepare a nuclear wavepacket in $|g\rangle$ which is different from its initial equilibrium configuration [12]. This will not happen as long as the impulsive limit is satisfied and the Condon approximation is valid.

[17] Had the population stayed only in $|I\rangle$ and $|O\rangle$ (and not in $|g\rangle$ via GSR), the number of unknowns would have been reduced to 12 real parameters [6].

[18] In fact, as we shall explain later, the two other potential peaks have negligible amplitudes even at $T > 0$.

[19] The smaller the condition number, the more stable the inversion; since some signals are directly proportional to certain elements of $\chi(T)$, the matrix is sparse and the inversion is stable.